Cellular organization of cortical barrel columns is whisker-specific

Hanno S. Meyer[a,b,1], Robert Egger[c,d,1], Jason M. Guest[a], Rita Foerster[e], Stefan Reissl[c], and Marcel Oberlaender[a,c,f,2]

[a]Digital Neuroanatomy, Max Planck Florida Institute for Neuroscience, Jupiter, FL 33458; [b]Department of Neurosurgery, Technical University of Munich, 81675 Munich, Germany; [c]Computational Neuroanatomy Group, Max Planck Institute for Biological Cybernetics, 72076 Tübingen, Germany; [d]Graduate School of Neural Information Processing, University of Tübingen, 72074 Tübingen, Germany; [e]Institute of Neuroscience, Technical University of Munich, 80802 Munich, Germany; and [f]Bernstein Center for Computational Neuroscience, 72076 Tübingen, Germany

Edited* by Peter L. Strick, University of Pittsburgh, Pittsburgh, PA, and approved September 20, 2013 (received for review July 4, 2013)

The cellular organization of the cortex is of fundamental importance for elucidating the structural principles that underlie its functions. It has been suggested that reconstructing the structure and synaptic wiring of the elementary functional building block of mammalian cortices, the cortical column, might suffice to reverse engineer and simulate the functions of entire cortices. In the vibrissal area of rodent somatosensory cortex, whisker-related "barrel" columns have been referred to as potential cytoarchitectonic equivalents of functional cortical columns. Here, we investigated the structural stereotypy of cortical barrel columns by measuring the 3D neuronal composition of the entire vibrissal area in rat somatosensory cortex and thalamus. We found that the number of neurons per cortical barrel column and thalamic "barreloid" varied substantially within individual animals, increasing by ∼2.5-fold from dorsal to ventral whiskers. As a result, the ratio between whisker-specific thalamic and cortical neurons was remarkably constant. Thus, we hypothesize that the cellular architecture of sensory cortices reflects the degree of similarity in sensory input and not columnar and/or cortical uniformity principles.

soma counts | NeuN | GAD67 | VPM | barrel cortex

Two major concepts of cortical neuronal organization have been proposed. Structurally, correlations between stereology-based measurements (1) of neuron density and cortical thickness resulted in the hypothesis of structural uniformity, arguing that the number of neurons beneath a square millimeter of cortical surface is constant and independent of cortical area and species (2, 3). Functionally, cortex is organized in a columnar fashion, reflecting similar neuronal activity along the vertical cortex axis in response to peripheral stimuli (4–8). Similar spatial extents of functional cortical columns in the horizontal plane, combined with the idea of cortical uniformity, resulted in the notion that a stereotypic columnar network may also represent the elementary structural building block of sensory cortices (9). In combination, the two concepts thus suggested a common organization of all sensory cortices, which led to reverse engineering and simulation efforts that build up large-scale network models of repeatedly occurring identical cortical circuits (10, 11).

The ideal model system for investigating columnar structure and function is the vibrissal area of rodent somatosensory cortex. There, "barrels" of neurons in layer 4 (L4) have been identified as somatotopically organized structural correlates of peripheral receptor organs (i.e., facial whiskers). Whisker/barrel columns have thus been regarded as both structural and functional elementary cortical units (12–14). To investigate the structural stereotypy of cortical barrel columns, independent of the drawbacks associated with stereology (i.e., extrapolations from small sampling regions), we decided to locate each excitatory and inhibitory neuron soma within the entire volume of interest. Using high-resolution, large-scale confocal microscopy (15) and automated image-processing routines (16), we found that the number of neurons per barrel column increased by ∼2.5-fold from columns that correspond to the dorsal facial whiskers (A-row) to columns corresponding to the ventral whiskers (E-row). Moreover, cortical thickness increased by ∼500 μm from A- to E-rows, resulting in whisker-specific laminar neuron profiles, layer locations, and thicknesses. Further, the distributions of excitatory and inhibitory neurons outside the L4 barrels were indistinguishable between barrel columns, the septa (the cortex separating the barrel columns) (14) and the dysgranular zones (DZ) surrounding the vibrissal cortex (17).

We performed the same analyses for the ventral posterior medial division (VPM) of rat thalamus, which provides whisker-specific input to the vibrissal cortex (18–20). Again, we found that the number of neurons per whisker (i.e., within so-called "barreloids") (21) was constant within a whisker row, but increased by ∼2.5-fold from the A- to the E-row. Consequently, the ratio between neurons per barrel (column) and respective barreloid was remarkably constant. This whisker-specific cellular organization is in contrast to the ideas of columnar and cortical uniformity, questioning the stereology-based concept that mammalian cortices are composed of stereotypical elementary building blocks.

Results

Across-Animal Variability in Rat Vibrissal Cortex. We measured the number of excitatory and inhibitory neurons within 24 barrel columns (α–δ, A1–E4) and the septa between them in four different rats (Fig. 1 *A*, *C*, and *D*; *SI Appendix*, Table S1). The average total number of neurons in this large portion of the vibrissal cortex was 529,715 ± 39,104 (mean ± SD). A fraction of 87% of the neurons in the vibrissal cortex were excitatory and 13% inhibitory. Extrapolating L4 barrel boundaries toward the pia and white matter (WM), 81% of all neurons were located within barrel columns and 19% in the septa between them. The total volume of this part of the vibrissal cortex after perfusion and fixation (22) was 6.60 ± 0.58 mm^3, which is consistent with

Significance

Cortical columns are thought to be the elementary functional building blocks of sensory cortices. Here we show that the cellular architecture of cortical "barrel" columns in rodent somatosensory cortex is not stereotypic, but specific for each whisker on the animals' snout. Our findings challenge the concepts underlying contemporary simulation efforts that build up large-scale network models of repeatedly occurring identical cortical circuits.

Author contributions: H.S.M. and M.O. designed research; H.S.M., R.E., J.M.G., R.F., and M.O. performed research; R.E., S.R., and M.O. contributed new reagents/analytic tools; H.S.M., R.E., and M.O. analyzed data; and H.S.M., R.E., and M.O. wrote the paper.

The authors declare no conflict of interest.

*This Direct Submission article had a prearranged editor.

Freely available online through the PNAS open access option.

[1]H.S.M. and R.E. contributed equally to this work.

[2]To whom correspondence should be addressed. E-mail: marcel.oberlaender@tuebingen.mpg.de.

This article contains supporting information online at www.pnas.org/lookup/suppl/doi:10.1073/pnas.1312691110/-/DCSupplemental.

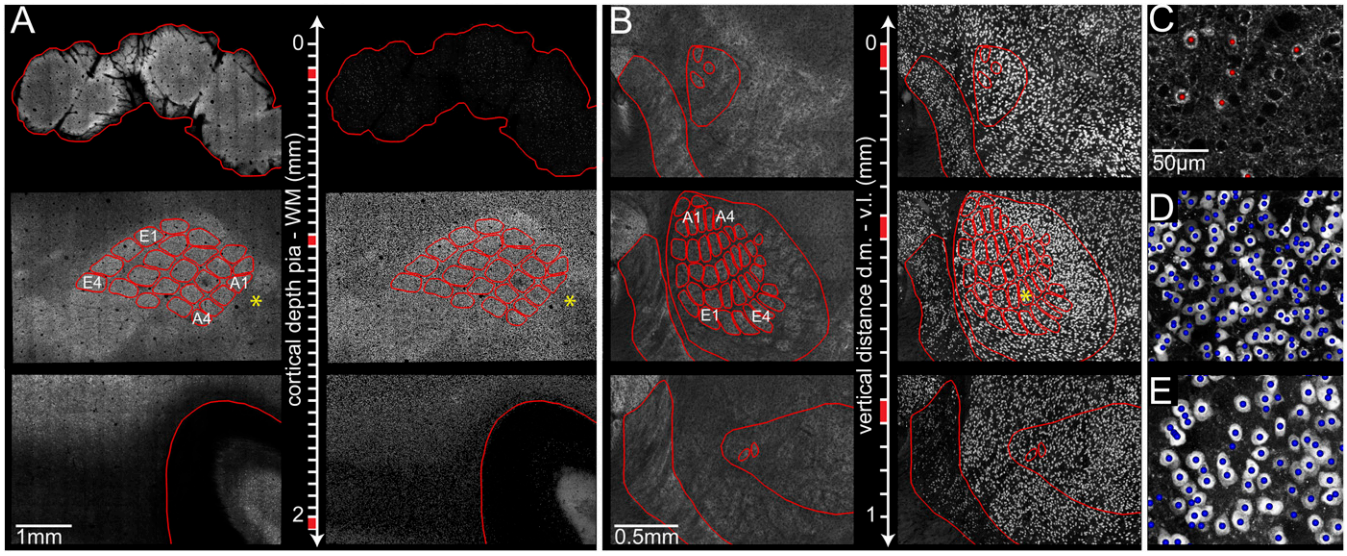

Fig. 1. Automated detection of all excitatory and inhibitory neuron somata in the vibrissal areas of rat somatosensory cortex and thalamus. (*A*) Large-scale, high-resolution confocal image stacks from 50-µm-thick brain sections, cut tangentially to the cortical surface from the pia to the WM. (*Left*) GAD67 projection images allow delineation of anatomical reference structures (red) in each section, such as pia, L4 barrels, and WM. (*Right*) NeuN projection images in the same sections. (*B*) Confocal image stacks from 50-µm-thick sections of vibrissal thalamus, cut tangentially from the dorsal medial (d.m.) to the ventral lateral (v.l.) direction. (*Left*) GAD67 projection images allow delineation of anatomical reference structures (red), such as RT (*Left*), VPM (*Right*), and individual barreloids. (*Right*) NeuN projection images in the same sections. (*C*) Optical section of GAD67 image stack from *A* (*) superimposed with landmarks representing automatically detected inhibitory somata (red). (*D*) NeuN-positive somata were automatically detected within the same area. (*E*) Area from *B* (*) with automatically detected NeuN-positive neuron somata. Brightness has been adjusted in all panels for visualization purposes.

previous measurements of the cortex geometry using cytochrome oxidase as a marker to reveal the barrels (6.53 ± 0.75 mm^3) (23). The across-animal variabilities in total neuron numbers (SD of mean: 7.4%) and volume (8.8%) were similar. Consequently, the average neuron density across the entire vibrissal cortex was remarkably preserved ($80{,}419 \pm 3{,}688$ mm^{-3}); the same was true

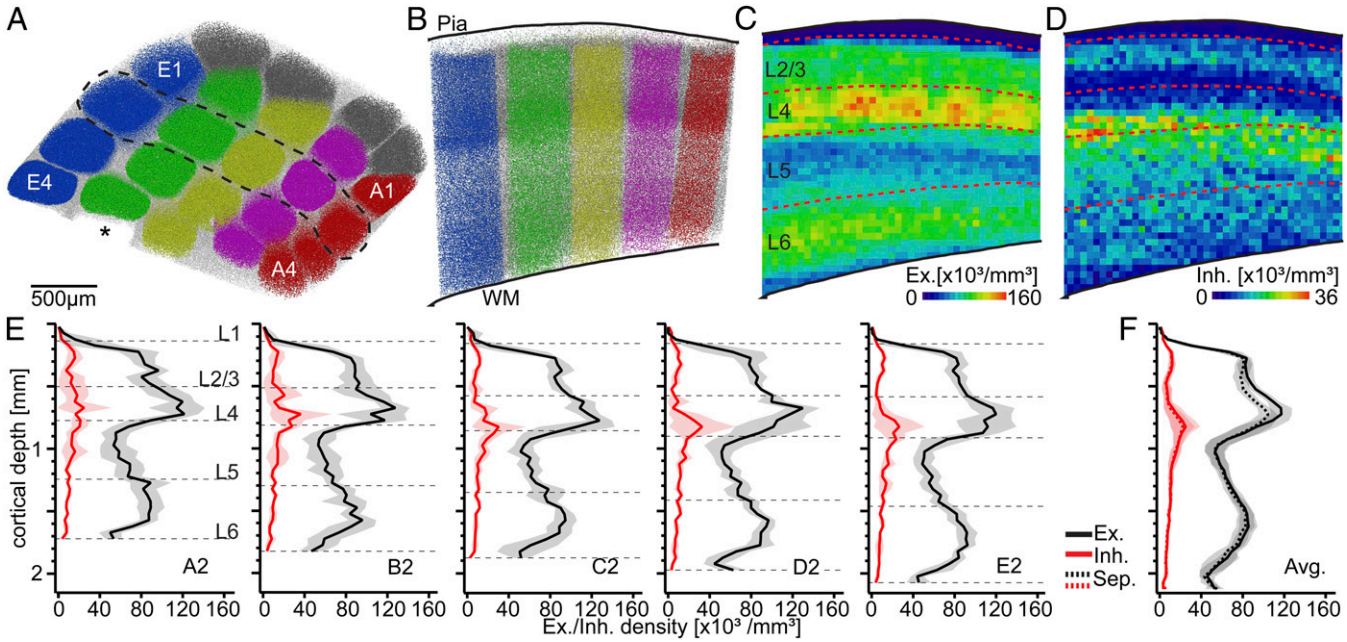

Fig. 2. Whisker-specific laminar cellular organization of rat vibrissal cortex. (*A*) Tangential view of all neuron somata in the vibrissal cortex of one animal. Somata are assigned to their closest barrel column [row colors: A (red), B (pink), C (yellow), D (green), E (blue), Greek arc (gray)] or to the septum (white). *D5 barrel column excluded from analysis. (*B*) Semicoronal view of the somata within the dashed region in *A*. A 3D reconstruction of pia and WM surfaces allows for determining the position of all neuron somata with respect to cytoarchitectonic layer borders (20). (*C*) A 2D average projection of the 3D excitatory neuron density. L4 barrels are clearly visible as segregated spots of high neuron density (24). (*D*) A 2D average projection of the 3D inhibitory neuron density. Segregation between barrels and septa is not evident. L2 and upper L5 are separable as bands of high inhibitory neuron density, as reported previously (22). (*E*) Average distribution of excitatory and inhibitory neuron somata along the vertical column axis for columns in arc-2. Shaded regions are ±1 SD. Dashed lines represent column-specific layer borders. (*F*) Average distribution of excitatory/inhibitory somata across all barrel columns and septa.

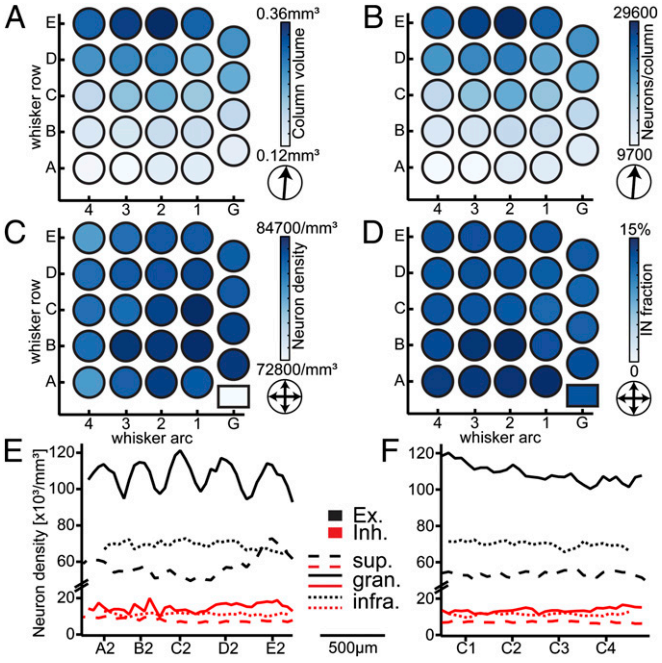

Fig. 3. Whisker-specific horizontal cellular organization of rat vibrissal cortex. (*A*) Average volume per barrel column based on the four vibrissal cortices analyzed, showing a significant increase from the A- to the E-row. (*B*) Average number of all neurons (excitatory and inhibitory) per barrel column, increasing from the A- to the E-row concomitantly with the column volume. (*C*) The average neuron density (excitatory and inhibitory) per barrel column is constant across the barrel field and larger than septal neuron density (box). (*D*) The average fraction of inhibitory neurons (IN) is similar across the barrel field and does not differ between columns and the septum (box). (*E*) The average distribution of excitatory/inhibitory neurons in different cortical layers, measured along arc-2 (from left to right: A2–E2), shows a clear separation into barrel columns and septa only in L4, where excitatory neurons delineate the barrels. (*F*) The average distribution of excitatory/inhibitory neurons in different cortical layers, measured along the C-row (from left to right: C1–C4), is not indicative of a separation between barrel columns and septa at the cellular level.

for the average density in columnar (82,402 ± 4,011 mm^{-3}) and septal (72,792 ± 2,419 mm^{-3}) regions, respectively. There was no difference between the neuron density in the septa between whisker rows (67,078 ± 4,751 mm^{-3}) and in the DZ surrounding the vibrissal cortex (68,236 ± 2,226 anterior medial to the E-row and 66,311 ± 1,084 mm^{-3} posterior lateral to the A-row; *SI Appendix*, Fig. S1).

Across-Animal Variability in Rat Vibrissal Thalamus. Labeling brain sections with GAD67 did not only reveal the columnar organization of rat vibrissal cortex, as previously reported (24), but also showed the segregation of VPM thalamus into barreloids (Fig. 1*B*). Using the same methodology as for the vibrissal cortex, we measured the number of excitatory and inhibitory neurons for the respective 24 barreloids in three different rats (Fig. 1*E*). The average total number of neurons in this portion of vibrissal thalamus was 9,963 ± 718. As for the vibrissal cortex, the variability in neuron numbers across animals was small (7.2%). All neurons in VPM thalamus were excitatory (i.e., GAD67 negative). The total volume of this part of vibrissal thalamus (i.e., convex hull around 24 barreloids; *Materials and Methods*) was 0.19 ± 0.03 mm^3, resulting in an average neuron density across the entire VPM of 52,494 ± 5,082 mm^{-3}. Densities in VPM within and above/below barreloids (51,507 ± 4,422 and 54,440 ± 6,559 mm^{-3}, respectively) were larger compared with the surrounding thalamic nuclei, with 49,680 ± 1,097 and 41,477 ± 3,612 mm^{-3} in nucleus reticularis (RT) and posterior medial nucleus (POm), respectively.

Whisker-Specific Laminar Organization. Each detected soma was assigned to its nearest barrel column or to the septum, respectively (Fig. 2 *A* and *B*). The resultant column/septum-specific 3D distribution of excitatory (Fig. 2*C*) and inhibitory somata (Fig. 2*D*) could thus be analyzed with respect to previously defined cytoarchitectonic layers (20). Cortical thickness (i.e., pia–WM distance along the respective vertical column axis) (23) increased substantially across the vibrissal cortex, being thinnest at the barrel column corresponding to the α-whisker (1,612 ± 36 µm) and thickest at the E3 whisker representation (2,089 ± 15 µm). The increase in cortical thickness was linear across whisker rows (linear regression: $R^2 = 0.99$, $P = 0.001$). Consequently, the density distributions of individual barrel columns were "stretched" along their respective vertical axis, resulting in column-specific depth locations and thicknesses of the respective cytoarchitectonic layers (Fig. 2*E*, dashed lines). In contrast, the height of the L4 barrel increased sublinearly ($R^2 = 0.9$, $P = 0.10$). Thus, the depth of granular L4 was more constant across the vibrissal cortex than the respective cortical thickness. For example, cortical thickness increased from the A2 (1,760 ± 39 µm) to the E2 column (2,063 ± 50 µm) by 303 µm, and the depth of the L4 peak (Gaussian approximation) shifted by 116 µm (from 647 to 763 µm below the pia surface), whereas the L5/6 peak shifted ∼2.4× more, i.e., by 275 µm (from 1,409 to 1,684 µm).

The density of excitatory and inhibitory neurons within each of the respective layers was remarkably constant across the vibrissal cortex. The average neuron density was 61,603 ± 3,721 mm^{-3} (SD of mean: 6.0%) within supragranular (s) L1–3, 122,931 ± 6,204 mm^{-3} (5.1%) within granular (g) L4 and 79,092 ± 5,383 mm^{-3} (6.8%) within infragranular (i) L5–6. The same was true for the average density in columnar (s: 63,878 ± 4,329; g: 126,145 ± 6,298; i: 79,424 ± 5,441 mm^{-3}) and septal (s: 56,061 ± 2,301; g: 111,293 ± 7,558; i: 77,090 ± 5,040 mm^{-3}) regions, respectively. Because neuron densities within a layer were constant, but layer depths and thicknesses changed across the vibrissal cortex, the numbers of excitatory and inhibitory neurons within cytoarchitectonic layers were highly whisker-specific (*SI Appendix*, Tables S2–S6).

The relative proportions of neurons per layer were, however, virtually identical for all barrel columns. A fraction of 24 ± 1% of all neurons within a barrel column were located within supragranular layers (L1: 0.5 ± 0.1%; L2/3: 23.3 ± 1.1%), 25.2 ± 2.0% in granular L4 and 51 ± 2% in infragranular layers (L5:24.2 ± 0.9%; L6: 26.8 ± 1.2%). The proportion of neurons within the L4 barrel was independent of the respective cortical thickness (Pearson's correlation coefficient: $r = 0.02$, two-tailed t test: $P = 0.93$) and significantly correlated with (i.e., predicted) the respective supragranular ($r = -0.46$, $P = 0.02$) and infragranular ($r = -0.77$, $P < 10^{-4}$) proportions. In contrast, supra- and infragranular proportions were uncorrelated ($r = 0.24$, $P = 0.26$). Consequently, the largely preserved vertical extent and depth location of the L4 barrels caused the constant laminar neuronal composition of cortical barrel columns, despite substantial whisker-specific increases in neuron numbers and cortical thickness.

Whisker-Specific Horizontal Organization. We calculated the direction of the gradient within the horizontal plane of the vibrissal cortex (Fig. 3, arrows) for the volume, neuron density, neuron number, and fraction of inhibitory neurons per barrel column, respectively. The horizontal gradient in column volume revealed a "rowish" organization of the vibrissal cortex (23). Barrel columns within the same whisker row displayed almost identical volumes (Table 1), whereas the column volume increased in an orderly manner from the A- toward the E-row by a factor of ∼2.5 (Fig. 3*A*; $P < 10^{-15}$, one-way ANOVA). In contrast, average neuron densities did not differ between columns, as indicated by the absence of a horizontal gradient across the vibrissal cortex (Fig. 3*C*; $P = 0.49$, two-tailed t test). Consequently, the average

Table 1. Whisker-specific organization in rat vibrissal cortex (S1) and thalamus (VPM)

Whisker	Volume S1	Neurons S1	Excitatory S1	Inhibitory S1	Volume VPM	Neurons VPM	Ratio S1/VPM
α	0.14 ± 0.03	11,781 ± 2,341	10,244 ± 2,235	1,536 ± 298	0.35 ± 0.05	186 ± 30	63
β	0.18 ± 0.02	15,002 ± 679	13,161 ± 857	1,841 ± 640	0.42 ± 0.06	199 ± 23	75
γ	0.24 ± 0.04	19,663 ± 1,857	17,270 ± 1,406	2,393 ± 857	0.56 ± 0.07	282 ± 11	70
δ	0.27 ± 0.03	21,919 ± 1,257	19,155 ± 1,363	2,764 ± 849	0.49 ± 0.06	246 ± 22	89*
A1	0.14 ± 0.02	11,832 ± 2,100	9,346 ± 1,480	1,675 ± 486	0.35 ± 0.05	196 ± 23	60
A2	0.14 ± 0.03	11,978 ± 2,415	9,424 ± 1,789	1,624 ± 370	0.31 ± 0.05	198 ± 28	61
A3	0.12 ± 0.01	9,741 ± 941	8,066 ± 990	1,351 ± 160	0.21 ± 0.04	132 ± 16	74
A4	0.12 ± 0.03	9,660 ± 2,190	8,228 ± 1,679	1,432 ± 655	0.14 ± 0.04	89 ± 20	108*
A-row	0.13 ± 0.01	10,803 ± 1,275	8,766 ± 719	1,521 ± 154	0.25 ± 0.09	154 ± 53	65 ± 8
B1	0.17 ± 0.03	14,387 ± 1,534	12,520 ± 1,806	1,866 ± 402	0.54 ± 0.06	295 ± 40	49
B2	0.17 ± 0.03	14,547 ± 1,888	11,953 ± 2,279	2,089 ± 392	0.54 ± 0.10	306 ± 26	47
B3	0.15 ± 0.03	12,999 ± 2,493	10,292 ± 1,951	1,741 ± 346	0.40 ± 0.09	227 ± 35	57
B4	0.15 ± 0.02	12,393 ± 1,949	10,726 ± 1,952	1,667 ± 242	0.26 ± 0.03	149 ± 8	83
B-row	0.16 ± 0.01	13,581 ± 1,054	11,373 ± 1,039	1,841 ± 185	0.43 ± 0.13	244 ± 73	59 ± 17
C1	0.21 ± 0.04	17,491 ± 2,406	15,459 ± 2,538	2,032 ± 551	0.64 ± 0.06	329 ± 12	53
C2	0.24 ± 0.02	19,707 ± 1,174	17,195 ± 1,545	2,511 ± 661	0.65 ± 0.06	350 ± 3	56
C3	0.22 ± 0.03	17,531 ± 1,496	15,273 ± 1,661	2,258 ± 435	0.47 ± 0.05	253 ± 19	69
C4	0.18 ± 0.03	14,918 ± 3,154	13,028 ± 3,075	1,890 ± 278	0.38 ± 0.03	218 ± 29	69
C-row	0.21 ± 0.02	17,412 ± 1,959	15,239 ± 1,709	2,173 ± 272	0.54 ± 0.13	287 ± 62	62 ± 8
D1	0.24 ± 0.01	20,078 ± 1,852	17,588 ± 2,191	2,489 ± 895	0.60 ± 0.06	286 ± 4	70
D2	0.28 ± 0.02	23,382 ± 1,484	20,377 ± 2,124	3,005 ± 844	0.64 ± 0.06	311 ± 7	75
D3	0.28 ± 0.04	22,696 ± 3,007	19,776 ± 3,304	2,920 ± 535	0.61 ± 0.12	296 ± 37	77
D4	0.26 ± 0.01	21,619 ± 760	18,862 ± 1,443	2,758 ± 686	0.53 ± 0.08	270 ± 26	80
D-row	0.27 ± 0.02	21,944 ± 1,440	19,151 ± 1,214	2,793 ± 227	0.60 ± 0.05	291 ± 17	76 ± 4
E1	0.31 ± 0.04	25,459 ± 1,879	22,183 ± 2,412	3,276 ± 836	0.65 ± 0.08	298 ± 55	85
E2	0.36 ± 0.06	29,563 ± 3,604	25,813 ± 4,133	3,750 ± 897	0.77 ± 0.15	346 ± 41	85
E3	0.34 ± 0.05	27,965 ± 4,344	24,391 ± 4,890	3,575 ± 698	0.86 ± 0.07	403 ± 33	69
E4	0.31 ± 0.05	24,671 ± 3,743	21,587 ± 4,118	3,085 ± 395	0.78 ± 0.06	361 ± 41	68
E-row	0.33 ± 0.02	26,914 ± 2,256	23,493 ± 1,961	3,421 ± 298	0.76 ± 0.08	352 ± 43	77 ± 10
Mean	0.22 ± 0.07	17,958 ± 5,800	15,497 ± 5,266	2,314 ± 697	0.51 ± 0.18	259 ± 78	68 ± 11

All numbers are mean ± SD (S1: $n = 4$; VPM: $n = 3$). Volumes in S1 and VPM are given in cubic millimeters and 10^{-2} mm^3, respectively.
*Barreloid Delta and A4 were excluded from the ratio analysis due to difficulties to identify their boundaries.

number of neurons per cortical barrel column followed the gradient in column volume, resulting in relatively constant neuron numbers for columns within the same whisker row (Table 1) and an orderly ~2.5-fold increase from the A- (10,803 ± 1,275 neurons) toward the E-row (26,914 ± 2,256 neurons) (Fig. 3*B*; $P < 10^{-15}$, one-way ANOVA).

Fig. 3*C* (lower right rectangle refers to the septum) indicates a significant drop in neuron density between barrel columns and septa. In contrast, the relative proportion of inhibitory neurons was independent of barrel column identity or septal location (Fig. 3*D*; $P = 0.65$, two-tailed t test). Moreover, the average 1D profiles in Fig. 2*F* revealed that the density of inhibitory neurons was nearly identical between columns (10,826 mm^{-3}) and septa (9,516 mm^{-3}). The distribution of excitatory neurons differed between columns and septa, but differences were limited to L4. There, the density of excitatory cells dropped from barrels to the septum by up to 17%, reflecting a decrease from ~120,000 to ~100,000 neurons per cubic millimeter. Fig. 3 *E* and *F* further illustrates this finding for the distribution of excitatory and inhibitory neurons within supragranular, granular, and infragranular layers, respectively. A significant separation between columns and septa was only evident for the distribution of excitatory neurons within granular L4 along the whisker arc (i.e., between whisker rows). Consequently, outside the L4 barrel, the cellular organization of excitatory and inhibitory neurons was virtually identical in barrel columns, septa, and the DZ surrounding the vibrissal cortex.

Organization Between Vibrissal Thalamus and Cortex. We also determined the neuron numbers, volumes, and densities of each individual VPM barreloid (Table 1 and Fig. 4 *A–C*). The relationship between barreloid volume and neuron density differed from the vibrissal cortex. The neuron density was not constant across VPM, but increased from the E1 toward the A4 barreloid by ~50%. Conversely, barreloid volume increased in the opposite direction from the A4 toward the E3 barreloid. Consequently, the number of neurons per barreloid was, similar to barrel columns, remarkably constant within a whisker row, increasing in an orderly manner by ~2.5-fold from the A- (154 ± 53 neurons) toward the E-row (352 ± 43 neurons; $P < 10^{-10}$). Thus, the ratio between the number of neurons per barrel column and the number of neurons within the respective barreloid was relatively constant (i.e., 68 ± 11). Because the depth locations and heights of the L4 barrels were more preserved than cortical thickness, we calculated the ratios between barrel columns and barreloids for supragranular, granular, and infragranular layers individually (Fig. 4 *D–F*). We found that the correlation between neuron numbers in the barreloid and the L4 barrel ($R^2 = 0.76$) exceeded the ones with the other layers ($R^2 = 0.68$ for supragranular and $R^2 = 0.62$ for infragranular layers), reflecting a remarkably constant neuron ratio of 18 ± 3 between each barrel and the respective barreloid (i.e., no significant gradient in neuron ratios, $P = 0.14$; two-tailed t test).

Discussion

Previous Studies of Cortical Cellular Organization. Several studies have investigated the cellular organization of sensory cortices, including rat vibrissal cortex (2, 3, 22, 24–26). Most of these studies were based on stereology, measuring local neuron densities and extrapolating them to larger reference volumes. Our results indicate that such approaches are problematic. First, neuron densities are not uniform, resulting in whisker-specific profiles along the vertical axis. Second, the sizes of the reference volumes (i.e., barrel columns) vary substantially across the vibrissal cortex, resulting in row-specific distributions within the

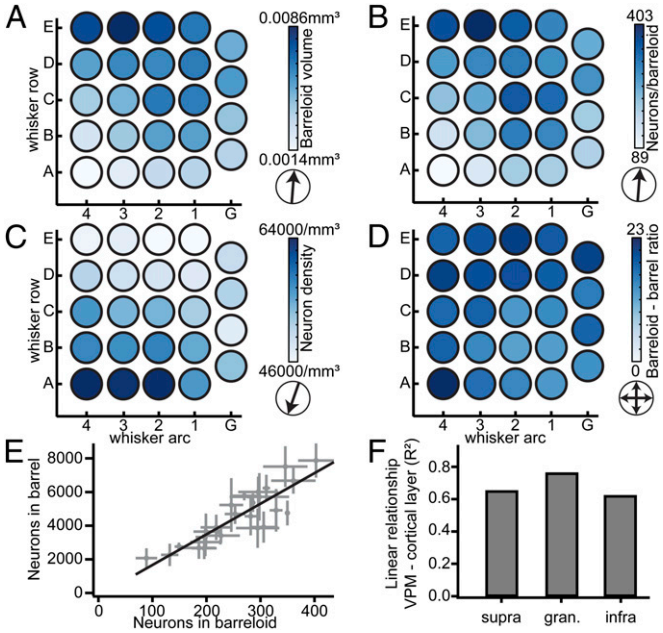

Fig. 4. The ratio between whisker-specific cortical and thalamic neurons is constant. (*A*) The average volume per barreloid across VPM increases from the A- to the E-row, as in vibrissal cortex. (*B*) The average number of neurons per barreloid also increases from the A- to the E-row. (*C*) The average neuron density per barreloid increases from the E- toward the A-row. (*D*) The average ratio between the number of neurons per barrel and corresponding barreloid is highly preserved. (*E*) Relationship between the number of neurons per barreloid in VPM and the number of neurons in the corresponding barrel is linear. Error bars are ±1 SD. (*F*) The linear relationship between neurons per barreloid and the respective number of target neurons in cortex is more pronounced for granular L4, compared with supra- and infragranular layers.

horizontal plane. Consequently, measuring the detailed 3D geometry of the entire vibrissal cortex, and detecting all neuron somata with respect to this anatomical reference frame, indicates that the variability across animals in neuron numbers and 3D distributions is much smaller compared with previous studies (e.g., ranging from neuron densities of 48,000 to 77,000 per cubic millimeter (25, 26)). Our automated counts further confirm previous manual (22, 24) and automated (27) counts of NeuN- and GAD67-positive neurons obtained for smaller datasets. Consequently, because neither the definition of a reference volume, nor the assumption of homogeneous neuron distributions within these volumes is required, we argue that our approach can be regarded as a robust alternative to stereology for revealing the cellular organization principles within any brain area of interest.

Cellular Organization Beyond Structural Uniformity. Stereology-based studies gave rise to idea of structural uniformity, suggesting that the number of neurons beneath the cortical surface is constant and independent of cortical area and species. The validity of this principle depends on whether differences in cortical thickness are compensated by changes in neuron densities. Measuring all these quantities directly, we showed that this hypothesis fails (*SI Appendix*, Fig. S2), at least for rat vibrissal cortex, which has been an integral part of the original studies that suggested structural uniformity (2, 3). Nevertheless, the structural uniformity principle gave rise to concepts about cortical organization in general. Though it is largely undisputed that cortex is subdivided into functional columns of various kinds (for a review, see ref. 28), the existence of anatomical counterparts remains controversial. Due to their unique anatomical segregation in L4, cortical barrel columns are usually regarded as potential candidates for such an anatomical equivalent. In combination with the structural uniformity principle, it was even suggested that understanding the structural and functional principles of one average cortical barrel column will serve as a template for understanding all cortical areas (9). This is arguably not the case. Our results show that neither does structural uniformity apply to rat vibrissal cortex, nor is the cellular organization of barrel columns identical within the same animal.

As an alternative organizational principle to columnar and cortical uniformity, we put forward the following hypothesis: The cellular organization of cortical barrel columns is primarily shaped by the similarity of sensory inputs from whiskers within the same row. For example, the large whiskers (arc 1–4) located in the E-row are closer to the ground and may touch it more frequently and/or are better suited to discriminate between textures than the corresponding whiskers within the A-row. In support of this idea are studies showing that sensory receptor densities around individual whiskers are proportional to the size of the corresponding "barrelettes" in brainstem (29), as well as to the number of neurons in the corresponding L4 barrel (30).

Despite substantial whisker-specific differences in total neuron numbers, some important aspects of the cellular composition of cortical barrel columns are highly preserved, e.g., the relative laminar neuronal composition, the fraction of inhibitory neurons, and, most importantly, the neuron ratio between the barrel and the respective barreloid. It remains to be investigated whether these preserved quantities are indicative of common elementary circuits and functions shared by all whiskers (e.g., for object localization), whereas progressively increasing neuron numbers may reflect additional functionalities and/or higher sensitivities depending on the whisker position with respect to the ground (e.g., for texture discrimination).

Conclusion

Using quantitative methods to reconstruct the cellular architecture of the entire rat vibrissal cortex and thalamus, we showed that cortical barrel columns and thalamic barreloids are organized in a whisker-specific manner. Our results are in line with previous hypotheses suggesting that information from the sensory sheet guides the features of cortical maps and that cortex is not constrained to form stereotypic columnar units (31). In case of rat vibrissal cortex, similar sensory input from whiskers within the same row may be manifested by adding a whisker-specific number of neurons to L4 during development (as reviewed in ref. 32; a process that is critically dependent on and guided by VPM input) (33), on top of a cellular architecture that is otherwise indistinguishable from the surrounding dysgranular cortices. Consequently, our findings argue against the views that cortical barrel columns represent stereotypic anatomical correlates of functional columns and that cortical organization follows a structural uniformity rule. It remains thus to be shown whether large-scale network models, based upon repeatedly occurring identical cortical columns (10), will elucidate general mechanisms that underlie cortical organization and sensory information processing.

Materials and Methods

Sample Preparation. Experimental procedures were conducted in accordance with the German Animal Welfare Act and approved by the Institutional Animal Care and Use Committee of the Max Planck Florida Institute for Neuroscience. Histology was conducted as reported previously (24). Briefly, Wistar rats (aged 28–29 d) were perfused transcardially, and brains were removed and fixed with paraformaldehyde. For neuron counting in cortex, 43–48 consecutive Vibratome sections of 50 μm thickness were cut tangentially to vibrissal cortex, and for neuron counting in thalamus, 15–18 sections 50 μm thick were cut semicoronally, i.e., approximately tangential to the barreloid field (34). Sections were double-immunolabeled for GAD67 (35–37) and NeuN (38).

Image Acquisition. Images were acquired using a prototype confocal laser scanning system (based on Leica Application Suite Advanced Fluorescence SP5; Leica Microsystems) equipped with a glycerol/oil immersion objective (HC PL APO 20×, 0.7 N.A.), a tandem scanning system (Resonance Scanner),

spectral detectors with hybrid technology (GaAsP photocathode), and mosaic scanning software [Matrix Screener (beta version), provided by Frank Sieckmann, Leica Microsystems]. Mosaic image stacks of volumes up to 5 × 3.5 × 0.05 mm (in cortex) and 3 × 3 × 0.05 mm (in thalamus) were acquired at a resolution of 0.36075 × 0.36075 × 0.5 μm per voxel (2.5× digital zoom, 8× line average, 8-kHz scanning speed, ∼15 × 10 and ∼9 × 9 fields of view in cortex and thalamus, respectively) for each consecutive brain section.

Image Processing. NeuN-positive somata were detected in each confocal image stack using a previously described automated counting algorithm (16). Each detected soma is represented by a 3D position landmark. The accuracy and robustness of the algorithms has been validated against manual counts performed by expert users (16, 24). For detection of GAD67-positive somata, we modified the previously reported automated algorithms to allow for reliable detection independent of the density of GAD67-positive boutons. The modifications are described in detail in *SI Appendix*. Note that in columns A1–3 and B2–3 of one animal, uneven staining prevented automatic separation between GAD67-positive and -negative somata in some portions of supragranular and granular layers. Excitatory/inhibitory neuron numbers of A1–3 and B2–3 in S1 (Tables 1; *SI Appendix*, Tables S3 and S4) are thus based on data from three, instead of four, animals.

Section Alignment. Outlines of anatomical structures (i.e., pia, barrels, and WM in cortex, and VPM, barreloids, and RT in thalamus) were manually drawn on median projections of the GAD67 image stacks for each section. Using the blood vessel patterns as reference landmarks, the contours and soma landmarks of adjacent cortical brain sections were aligned manually by rigid transformations using ZIBAmira software (39), as reported previously (23). Contours and soma landmarks from thalamic sections were aligned analogously using the outlines of RT and individual barreloids as reference structures.

Cortical and Thalamic 3D Reference Volumes. The 3D reconstruction of cortex geometry was performed as described previously (23). Briefly, barrel outlines and orientations were reconstructed in 3D from the 2D contours. Barrel columns were reconstructed by extrapolating the L4 barrel outlines along the vertical column axes toward the pia and WM surfaces (compensating for overlapping columns in deep layers) (23). The border between vibrissal cortex and DZ was defined based on the convex hull around all reconstructed barrel columns. Reference volumes in the DZ were selected manually and, on average, comprised volumes of ∼2.5 mm^3. Barreloids in VPM thalamus were reconstructed from outlines using 3D Delaunay triangulation. Reference volumes in POm were selected manually and, on average, comprised volumes of ∼0.4 mm^3.

Neuron Densities and Absolute Neuron Numbers. Soma distributions were scaled to a slice thickness of 50 μm. Each neuron soma was assigned to the closest barrel column/barreloid or to septum, as well as to supragranular, granular, or infragranular cortical layers (i.e., above, within, or below the L4 barrels). Total neuron counts for individual columns/barreloids were obtained by summing up all neuron somata assigned to the same column/barreloid. Vertical density profiles were computed in 50-μm steps along the respective vertical column axes. Density profiles along the row or arc were obtained by registration to a standardized model of rat vibrissal cortex (23).

Statistical and Analysis Routines. If not mentioned otherwise, all computations were performed using custom-written software with the Insight Segmentation and Registration Toolkit and Visualization Toolkit libraries in C++ (40).

ACKNOWLEDGMENTS. We thank Bert Sakmann, Hans-Joachim Wagner, and the entire staff of the Anatomy Institute of the University of Tubingen for their generous support. Funding was provided by the Max Planck Florida Institute for Neuroscience (H.S.M., J.M.G., and M.O.), the Studienstiftung des deutschen Volkes (R.E.), the Bernstein Center for Computational Neuroscience, funded by German Federal Ministry of Education and Research Grant BMBF/FKZ 01GQ1002 (to R.E. and M.O.), the Max Planck Institute for Biological Cybernetics (R.E. and M.O.), the Werner Reichardt Center for Integrative Neuroscience (M.O.), and the Max Planck Institute of Neurobiology (R.F. and S.R.).

1. Sterio DC (1984) The unbiased estimation of number and sizes of arbitrary particles using the disector. *J Microsc* 134(Pt 2):127–136.
2. Carlo CN, Stevens CF (2013) Structural uniformity of neocortex, revisited. *Proc Natl Acad Sci USA* 110(4):1488–1493.
3. Rockel AJ, Hiorns RW, Powell TP (1980) The basic uniformity in structure of the neocortex. *Brain* 103(2):221–244.
4. Hubel DH, Wiesel TN (1959) Receptive fields of single neurones in the cat's striate cortex. *J Physiol* 148:574–591.
5. Hubel DH, Wiesel TN (1968) Receptive fields and functional architecture of monkey striate cortex. *J Physiol* 195(1):215–243.
6. Hubel DH, Wiesel TN (1969) Anatomical demonstration of columns in the monkey striate cortex. *Nature* 221(5182):747–750.
7. Hubel DH, Wiesel TN, Stryker MP (1977) Orientation columns in macaque monkey visual cortex demonstrated by the 2-deoxyglucose autoradiographic technique. *Nature* 269(5626):328–330.
8. Mountcastle VB, Davies PW, Berman AL (1957) Response properties of neurons of cat's somatic sensory cortex to peripheral stimuli. *J Neurophysiol* 20(4):374–407.
9. Markram H (2006) The blue brain project. *Nat Rev Neurosci* 7(2):153–160.
10. Hill SL, Wang Y, Riachi I, Schürmann F, Markram H (2012) Statistical connectivity provides a sufficient foundation for specific functional connectivity in neocortical neural microcircuits. *Proc Natl Acad Sci USA* 109(42):E2885–E2894.
11. Izhikevich EM, Edelman GM (2008) Large-scale model of mammalian thalamocortical systems. *Proc Natl Acad Sci USA* 105(9):3593–3598.
12. Armstrong-James M, Fox K, Das-Gupta A (1992) Flow of excitation within rat barrel cortex on striking a single vibrissa. *J Neurophysiol* 68(4):1345–1358.
13. Simons DJ (1978) Response properties of vibrissa units in rat SI somatosensory neocortex. *J Neurophysiol* 41(3):798–820.
14. Woolsey TA, Van der Loos H (1970) The structural organization of layer IV in the somatosensory region (SI) of mouse cerebral cortex. The description of a cortical field composed of discrete cytoarchitectonic units. *Brain Res* 17(2):205–242.
15. Kleinfeld D, et al. (2011) Large-scale automated histology in the pursuit of connectomes. *J Neurosci* 31(45):16125–16138.
16. Oberlaender M, et al. (2009) Automated three-dimensional detection and counting of neuron somata. *J Neurosci Methods* 180(1):147–160.
17. Brett-Green BA, Chen-Bee CH, Frostig RD (2001) Comparing the functional representations of central and border whiskers in rat primary somatosensory cortex. *J Neurosci* 21(24):9944–9954.
18. Brecht M, Sakmann B (2002) Whisker maps of neuronal subclasses of the rat ventral posterior medial thalamus, identified by whole-cell voltage recording and morphological reconstruction. *J Physiol* 538(Pt 2):495–515.
19. Bruno RM, Sakmann B (2006) Cortex is driven by weak but synchronously active thalamocortical synapses. *Science* 312(5780):1622–1627.
20. Oberlaender M, et al. (2012) Cell type-specific three-dimensional structure of thalamocortical circuits in a column of rat vibrissal cortex. *Cereb Cortex* 22(10):2375–2391.
21. Land PW, Buffer SA, Jr., Yaskosky JD (1995) Barreloids in adult rat thalamus: Three-dimensional architecture and relationship to somatosensory cortical barrels. *J Comp Neurol* 355(4):573–588.
22. Meyer HS, et al. (2011) Inhibitory interneurons in a cortical column form hot zones of inhibition in layers 2 and 5A. *Proc Natl Acad Sci USA* 108(40):16807–16812.
23. Egger R, Narayanan RT, Helmstaedter M, de Kock CP, Oberlaender M (2012) 3D reconstruction and standardization of the rat vibrissal cortex for precise registration of single neuron morphology. *PLOS Comput Biol* 8(12):e1002837.
24. Meyer HS, et al. (2010) Number and laminar distribution of neurons in a thalamocortical projection column of rat vibrissal cortex. *Cereb Cortex* 20(10):2277–2286.
25. Beaulieu C (1993) Numerical data on neocortical neurons in adult rat, with special reference to the GABA population. *Brain Res* 609(1-2):284–292.
26. Keller A, Carlson GC (1999) Neonatal whisker clipping alters intracortical, but not thalamocortical projections, in rat barrel cortex. *J Comp Neurol* 412(1):83–94.
27. Tsai PS, et al. (2009) Correlations of neuronal and microvascular densities in murine cortex revealed by direct counting and colocalization of nuclei and vessels. *J Neurosci* 29(46):14553–14570.
28. Mountcastle VB (1997) The columnar organization of the neocortex. *Brain* 120(Pt 4): 701–722.
29. Ma PM (1991) The barrelettes—architectonic vibrissal representations in the brainstem trigeminal complex of the mouse. 1. Normal structural organization. *J Comp Neurol* 309(2):161–199.
30. Lee KJ, Woolsey TA (1975) A proportional relationship between peripheral innervation density and cortical neuron number in the somatosensory system of the mouse. *Brain Res* 99(2):349–353.
31. Catania KC (2002) Barrels, stripes, and fingerprints in the brain—implications for theories of cortical organization. *J Neurocytol* 31(3–5):347–358.
32. Inan M, Crair MC (2007) Development of cortical maps: Perspectives from the barrel cortex. *Neuroscientist* 13(1):49–61.
33. Li H, et al. (2013) Laminar and columnar development of barrel cortex relies on thalamocortical neurotransmission. *Neuron* 79(5):970–986.
34. Haidarliu S, Ahissar E (2001) Size gradients of barreloids in the rat thalamus. *J Comp Neurol* 429(3):372–387.
35. Julien JF, Samama P, Mallet J (1990) Rat brain glutamic acid decarboxylase sequence deduced from a cloned cDNA. *J Neurochem* 54(2):703–705.
36. Kaufman DL, McGinnis JF, Krieger NR, Tobin AJ (1986) Brain glutamate decarboxylase cloned in lambda gt-11: Fusion protein produces gamma-aminobutyric acid. *Science* 232(4754):1138–1140.
37. Kobayashi Y, Kaufman DL, Tobin AJ (1987) Glutamic acid decarboxylase cDNA: Nucleotide sequence encoding an enzymatically active fusion protein. *J Neurosci* 7(9):2768–2772.
38. Mullen RJ, Buck CR, Smith AM (1992) NeuN, a neuronal specific nuclear protein in vertebrates. *Development* 116(1):201–211.
39. FEI Visualization Sciences Group (2013) Amira 5.4 Software (FEI, Burlington, MA).
40. Ibáñez L, et al. (2003) *The ITK Software Guide* (Kitware, Inc., Clifton Park, NY).

Supplementary Figures

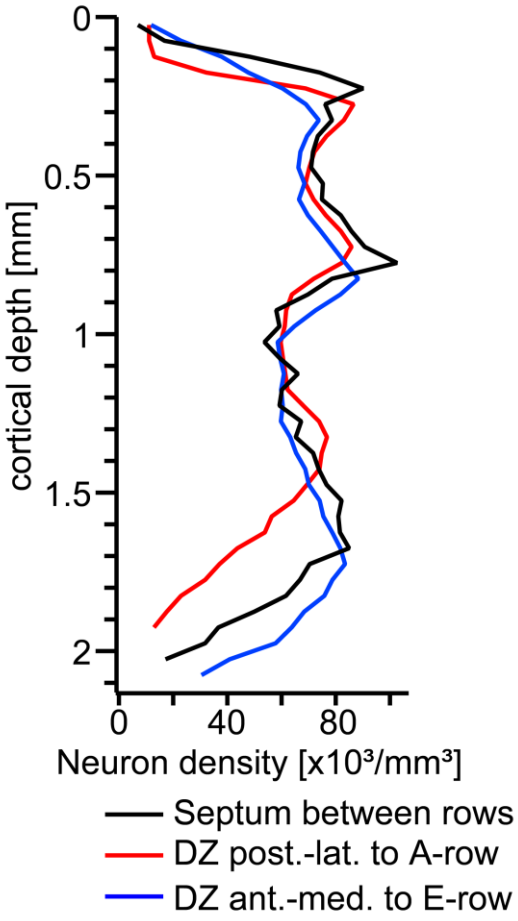

Figure S1: Neuron distributions in septa between whisker rows are indistinguishable from dysgranular zones surrounding rat vibrissal cortex. Average vertical neuron density profiles measured exclusively in the septum between rows (black; 2x between C- and D-rows, 1x between D- and E-rows), the dysgranular zone posterior-lateral to the A-row (red) and anterior-medial to the E-row (blue).

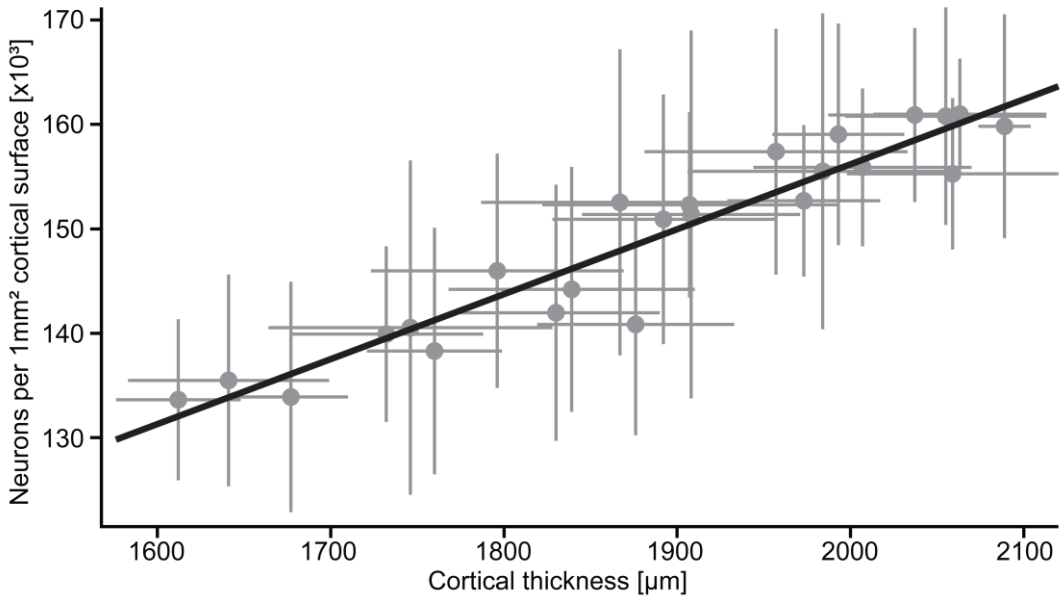

Figure S2: Changes in cortical thickness are not compensated by neuron densities as suggested by 'structural uniformity'. Average number of neurons underneath 1mm² of cortical surface as a function of cortical thickness. Calculated for individual barrel columns by dividing the average number of neurons inside the barrel columns by the average cross-sectional area of the barrel column. Cortical thickness is the pia-WM distance measured along the vertical column axis. Pearson's correlation coefficient: $r=0.95$, $p<0.0001$ (two-sided t-test). Error bars are ±1 SD.

Supplementary Tables

Supplementary Table 1: Across-animal-variability in cellular organization of rat vibrissal cortex (S1) and thalamus (VPM).

α-δ, A1-E4	Cortex	SD (%)	Thalamus	SD (%)
neurons	529,715 ± 39,104	7	9,963 ± 718	7
excitatory	460,981 ± 51,583	11	9,963 ± 718	7
inhibitory	68,734 ± 14,160	21		
columns	430,980 ± 36,830	9	6,225 ± 173	3
septa	98,735 ± 10,907	11	3,735 ± 657	18
volume (mm^3)	6.60 ± 0.58	9	0.19 ± 0.03	16
columns	5.24 ± 0.51	10	0.12 ± 0.01	8
septa	1.36 ± 0.16	12	0.07 ± 0.02	29
density (mm^{-3})	80,419 ± 3,688	5	52,494 ± 5,082	10
columns	82,402 ± 4,011	5	51,507 ± 4,422	9
septa	72,792 ± 2,419	3	54,440 ± 6,559	12
DZ*/RT	68,236 ± 2,226	3	49,680 ± 1,097	2
DZ$^{\$}$/POm	66,311 ± 1,084	2	41,477 ± 3,612	9

All numbers are mean ± SD (S1: n=4, VPM: n=3). *denotes density in DZ anterior-medial to the E-row in vibrissal cortex; n=2. $^{\$}$denotes density in DZ posterior-lateral to the A-row in vibrissal cortex; n=3.

Supplementary Table 2: Cellular composition of Layer 1 (L1).

	L1-L2/3 border [µm]	L1 neurons	L1 exc. neurons	L1 inh. neurons	L1 fraction [%]
α	139 ± 20	56 ± 27	32 ± 19	23 ± 18	0.5
β	143 ± 13	55 ± 15	22 ± 6	32 ± 15	0.4
γ	151 ± 17	85 ± 22	37 ± 16	48 ± 11	0.4
δ	152 ± 9	94 ± 38	46 ± 25	48 ± 23	0.4
A1	140 ± 11	58 ± 36	43 ± 36	15 ± 9	0.5
A2	137 ± 8	103 ± 131	81 ± 121	22 ± 12	0.8
A3	147 ± 21	74 ± 62	43 ± 76	31 ± 18	0.8
A4	154 ± 22	55 ± 35	24 ± 17	31 ± 25	0.6
A-row	145 ± 8	72 ± 22	48 ± 24	25 ± 8	0.6 ± 0.2
B1	139 ± 10	94 ± 22	58 ± 10	37 ± 18	0.7
B2	140 ± 17	101 ± 52	74 ± 51	27 ± 7	0.7
B3	145 ± 21	69 ± 54	48 ± 55	21 ± 8	0.5
B4	151 ± 20	63 ± 29	38 ± 33	25 ± 9	0.5
B-row	144 ± 5	82 ± 19	54 ± 15	27 ± 7	0.6 ± 0.1
C1	139 ± 17	68 ± 10	29 ± 12	39 ± 13	0.4
C2	157 ± 14	142 ± 42	91 ± 41	51 ± 17	0.7
C3	154 ± 15	95 ± 24	58 ± 30	37 ± 12	0.6
C4	158 ± 8	60 ± 30	34 ± 18	25 ± 19	0.4
C-row	152 ± 9	91 ± 37	53 ± 28	38 ± 11	0.5 ± 0.2
D1	154 ± 19	90 ± 11	42 ± 18	48 ± 13	0.4
D2	157 ± 16	128 ± 25	64 ± 2	64 ± 27	0.6
D3	159 ± 14	149 ± 37	83 ± 28	66 ± 42	0.7
D4	161 ± 26	105 ± 49	67 ± 48	38 ± 19	0.5
D-row	158 ± 3	118 ± 26	64 ± 17	54 ± 13	0.5 ± 0.1
E1	158 ± 7	123 ± 20	63 ± 21	60 ± 15	0.5
E2	160 ± 11	153 ± 37	86 ± 38	67 ± 15	0.5
E3	159 ± 15	148 ± 47	90 ± 34	58 ± 20	0.5
E4	155 ± 23	171 ± 60	114 ± 52	57 ± 13	0.7
E-row	158 ± 2	149 ± 20	88 ± 21	60 ± 5	0.6 ± 0.1
Average	150 ± 8	97 ± 36	57 ± 25	40 ± 16	0.5 ± 0.1

Fraction: relative to average total number of neurons in the same column. Layer borders were determined using previously determined cell type-specific vertical extents (1). Specifically, the border of L4 spiny stellate neurons coincided with the GAD67-based definition of the respective barrel top and bottom, as well as with the excitatory neuron density peak (Gaussian approximation ± full width half maximum; see (2)). Thus, the L2/3-L4 as well as the L4-L5 borders were consistent across cytoarchitectonic-, cell type- and neuron density-based definitions. The remaining layer borders were determined for each barrel column individually using linear interpolations of cell type borders determined for the D2 barrel column. Interpolations were performed between the pia and respective barrel top, and between the barrel bottom and respective WM for each barrel column individually. Within the first ~100µm below the pia, virtually all neurons are inhibitory, as reported previously (3). The depth location of the first excitatory neurons below the pia surface may thus be used as an alternative definition of the L1/2 layer border (3), compared to the cell type borders (~150µm) (1) used in the present study.

Supplementary Table 3: Cellular composition of Layer 2/3 (L2/3).

	L2/3-L4 border [µm]	L2/3 neurons	L2/3 exc. neurons	L2/3 inh. neurons	L2/3 fraction [%]
α	509 ± 72	2,958 ± 989	2,663 ± 935	295 ± 90	24.9
β	523 ± 48	3,580 ± 457	3,221 ± 429	359 ± 100	23.9
γ	552 ± 62	4,899 ± 219	4,429 ± 239	470 ± 141	25.1
δ	555 ± 33	5,026 ± 319	4,560 ± 227	466 ± 93	23.0
A1	513 ± 39	2,977 ± 891	2,294 ± 542	310 ± 148	24.8
A2	502 ± 28	2,743 ± 680	2,067 ± 281	365 ± 204	22.9
A3	540 ± 78	2,339 ± 459	1,894 ± 214	279 ± 178	24.2
A4	564 ± 79	2,509 ± 829	2,187 ± 673	322 ± 200	25.7
A-row	530 ± 28	2,642 ± 278	2,110 ± 171	319 ± 35	24.4 ± 1.2
B1	508 ± 37	3,296 ± 269	2,922 ± 311	374 ± 105	23.1
B2	512 ± 61	3,404 ± 1,044	2,568 ± 579	356 ± 92	23.1
B3	531 ± 77	2,918 ± 1,038	2,100 ± 437	326 ± 116	22.1
B4	552 ± 73	2,797 ± 681	2,496 ± 665	301 ± 77	22.4
B-row	526 ± 20	3,104 ± 292	2,522 ± 337	339 ± 33	22.7 ± 0.5
C1	511 ± 63	3,869 ± 564	3,464 ± 630	405 ± 92	22.3
C2	576 ± 52	4,758 ± 358	4,273 ± 445	485 ± 140	24.2
C3	564 ± 54	3,887 ± 902	3,455 ± 903	432 ± 37	22.0
C4	580 ± 30	3,424 ± 622	3,099 ± 650	326 ± 31	23.1
C-row	558 ± 32	3,984 ± 558	3,573 ± 497	412 ± 67	22.9 ± 1.0
D1	564 ± 71	4,717 ± 1,109	4,268 ± 1,123	450 ± 128	23.3
D2	575 ± 57	5,458 ± 351	4,936 ± 421	522 ± 99	23.4
D3	582 ± 51	5,117 ± 947	4,609 ± 1,021	508 ± 85	22.4
D4	589 ± 97	4,927 ± 977	4,439 ± 1,045	488 ± 131	22.7
D-row	577 ± 11	5,055 ± 314	4,563 ± 285	492 ± 31	23.0 ± 0.5
E1	579 ± 26	5,839 ± 693	5,279 ± 741	560 ± 50	22.9
E2	584 ± 39	6,751 ± 1,097	6,107 ± 1,147	644 ± 54	22.8
E3	584 ± 55	6,164 ± 957	5,520 ± 969	644 ± 91	22.2
E4	569 ± 84	5,407 ± 1,604	4,852 ± 1,542	554 ± 93	21.6
E-row	579 ± 7	6,040 ± 566	5,439 ± 524	601 ± 50	22.4 ± 0.6
Average	551 ± 30	4,157 ± 1,267	3,654 ± 1,244	427 ± 109	23.3 ± 1.1

The inhibitory neuron distribution in rat vibrissal cortex (see Fig. 2D) is indicative of a separation of L2/3 into L2 (defined by high inhibitory neuron density) and L3 (defined by low inhibitory neuron density), as reported previously (3).

Supplementary Table 4: Cellular composition of Layer 4 (L4).

	L4-L5 border [µm]	L4 neurons	L4 exc. neurons	L4 inh. neurons	L4 fraction [%]
α	746 ± 35	2,674 ± 646	2,324 ± 606	350 ± 52	22.9
β	770 ± 46	3,645 ± 1,070	3,290 ± 1,061	354 ± 129	24.2
γ	794 ± 46	4,562 ± 1,134	4,117 ± 1,055	445 ± 251	23.0
δ	842 ± 36	5,227 ± 1,597	4,634 ± 1,630	592 ± 266	23.6
A1	749 ± 34	2,659 ± 645	2,328 ± 811	460 ± 117	22.8
A2	774 ± 32	3,027 ± 834	2,686 ± 1,029	390 ± 20	25.4
A3	802 ± 26	2,268 ± 664	2,063 ± 771	312 ± 40	23.2
A4	801 ± 30	2,072 ± 580	1,781 ± 517	291 ± 145	21.4
A-row	782 ± 25	2,506 ± 424	2,214 ± 386	363 ± 77	23.2 ± 1.7
B1	791 ± 46	3,856 ± 1,177	3,415 ± 1,206	441 ± 36	26.4
B2	810 ± 14	3,913 ± 923	3,647 ± 967	612 ± 263	27.2
B3	846 ± 33	3,407 ± 442	3,080 ± 576	463 ± 152	26.9
B4	834 ± 51	2,757 ± 232	2,369 ± 373	388 ± 147	22.6
B-row	820 ± 25	3,483 ± 534	3,128 ± 557	476 ± 96	25.8 ± 2.1
C1	820 ± 28	4,911 ± 1,264	4,462 ± 1,286	449 ± 199	27.8
C2	855 ± 25	4,756 ± 734	4,184 ± 859	572 ± 229	24.1
C3	896 ± 35	4,688 ± 587	4,105 ± 600	583 ± 145	26.9
C4	904 ± 47	3,900 ± 753	3,389 ± 717	511 ± 181	26.4
C-row	869 ± 39	4,564 ± 452	4,035 ± 457	529 ± 62	26.3 ± 1.6
D1	889 ± 40	5,363 ± 545	4,703 ± 959	660 ± 481	26.9
D2	900 ± 50	6,233 ± 796	5,391 ± 1,267	842 ± 588	26.6
D3	918 ± 45	6,006 ± 911	5,289 ± 1,100	717 ± 189	26.5
D4	934 ± 72	5,777 ± 269	5,066 ± 415	711 ± 435	26.8
D-row	910 ± 20	5,844 ± 371	5,112 ± 305	732 ± 77	26.7 ± 0.2
E1	864 ± 50	5,712 ± 1,412	5,049 ± 1,495	664 ± 421	22.3
E2	912 ± 49	7,507 ± 1,208	6,636 ± 1,430	871 ± 423	25.5
E3	951 ± 64	7,868 ± 1,017	6,881 ± 1,393	987 ± 454	28.3
E4	924 ± 73	6,673 ± 768	5,966 ± 970	706 ± 356	27.2
E-row	913 ± 36	6,940 ± 959	6,133 ±820	807 ± 150	25.8 ± 2.6
Average	847 ± 62	4,561 ± 1,626	4,036 ± 1,429	557 ± 186	25.2 ± 2.0

Supplementary Table 5: Cellular composition of Layer 5 (L5).

	L5-L6 border [µm]	L5 neurons	L5 exc. neurons	L5 inh. neurons	L5 fraction [%]
α	1,158 ± 33	2,856 ± 575	2,323 ± 644	533 ± 202	24.3
β	1,185 ± 35	3,563 ± 194	2,876 ± 389	687 ± 347	23.8
γ	1,247 ± 42	4,706 ± 657	3,758 ± 266	948 ± 402	23.9
δ	1,330 ± 28	5,044 ± 258	3,961 ± 486	1,083 ± 424	23.1
A1	1,191 ± 19	2,968 ± 634	2,427 ± 642	541 ± 185	25.1
A2	1,243 ± 8	2,910 ± 704	2,392 ± 770	519 ± 166	24.3
A3	1,296 ± 40	2,441 ± 292	2,011 ± 399	429 ± 108	25.1
A4	1,313 ± 35	2,554 ± 456	2,027 ± 222	526 ± 272	26.6
A-row	1,261 ± 55	2,718 ± 260	2,214 ± 226	504 ± 51	25.3 ± 1.0
B1	1,239 ± 32	3,357 ± 165	2,690 ± 460	667 ± 301	23.5
B2	1,295 ± 23	3,567 ± 471	2,907 ± 610	660 ± 201	24.6
B3	1,351 ± 42	3,210 ± 554	2,664 ± 658	546 ± 196	24.8
B4	1,368 ± 63	3,220 ± 529	2,620 ± 579	599 ± 189	26.0
B-row	1,314 ± 59	3,338 ± 167	2,720 ± 128	618 ± 57	24.7 ± 1.0
C1	1,285 ± 27	4,098 ± 395	3,360 ± 431	737 ± 279	23.5
C2	1,349 ± 32	4,836 ± 302	3,929 ± 453	907 ± 323	24.6
C3	1,414 ± 34	4,208 ± 453	3,427 ± 570	780 ± 296	24.0
C4	1,429 ± 46	3,591 ± 748	2,955 ± 749	636 ± 206	24.1
C-row	1,369 ± 66	4,183 ± 511	3,418 ± 400	765 ± 112	24.1 ± 0.4
D1	1,373 ± 45	4,607 ± 762	3,764 ± 793	843 ± 271	22.8
D2	1,411 ± 28	5,574 ± 572	4,548 ± 579	1,026 ± 293	23.8
D3	1,451 ± 19	5,325 ± 379	4,277 ± 531	1,048 ± 341	23.6
D4	1,468 ± 55	5,114 ± 315	4,164 ± 304	950 ± 284	23.7
D-row	1,426 ± 42	5,155 ± 411	4,189 ± 326	967 ± 93	23.5 ± 0.4
E1	1,401 ± 30	6,295 ± 619	4,990 ± 678	1,304 ± 374	24.7
E2	1,460 ± 38	6,959 ± 862	5,563 ± 1,020	1,396 ± 413	23.5
E3	1,493 ± 34	6,505 ± 788	5,312 ± 921	1,193 ± 308	23.4
E4	1,464 ± 47	5,877 ± 597	4,751 ± 799	1,125 ± 251	24.0
E-row	1,455 ± 38	6,409 ± 450	5,154 ± 357	1,255 ± 120	23.9 ± 0.6
Average	1,342 ± 98	4,308 ± 1,319	3,487 ± 1,050	820 ± 274	24.2 ± 0.9

Supplementary Table 6: Cellular composition of Layer 6 (L6).

	L6-WM border [µm]	L6 neurons	L6 exc. neurons	L6 inh. neurons	L6 fraction [%]
α	1,612 ± 36	3,238 ± 654	2,903 ± 586	335 ± 79	27.5
β	1,641 ± 58	4,160 ± 421	3,751 ± 328	408 ± 109	27.5
γ	1,746 ± 82	5,411 ± 776	4,928 ± 653	483 ± 132	27.5
δ	1,867 ± 80	6,529 ± 448	5,953 ± 329	575 ± 157	29.9
A1	1,677 ± 33	3,171 ± 570	2,862 ± 564	309 ± 45	26.9
A2	1,760 ± 39	3,195 ± 693	2,895 ± 628	300 ± 86	26.6
A3	1,839 ± 71	2,619 ± 381	2,371 ± 356	248 ± 43	26.8
A4	1,876 ± 57	2,471 ± 663	2,210 ± 592	261 ± 73	25.6
A-row	1,788 ± 88	2,864 ± 373	2,584 ± 346	279 ± 30	26.5 ± 0.6
B1	1,732 ± 56	3,783 ± 327	3,436 ± 290	347 ± 56	26.4
B2	1,830 ± 60	3,563 ± 604	3,209 ± 551	354 ± 80	24.4
B3	1,908 ± 63	3,396 ± 964	3,067 ± 880	328 ± 104	25.8
B4	1,957 ± 76	3,557 ± 767	3,202 ± 722	354 ± 85	28.5
B-row	1,857 ± 98	3,575 ± 159	3,229 ± 153	346 ± 12	26.3 ± 1.7
C1	1,796 ± 73	4,546 ± 658	4,144 ± 588	402 ± 87	26.0
C2	1,892 ± 64	5,215 ± 431	4,718 ± 455	497 ± 77	26.4
C3	1,984 ± 78	4,654 ± 430	4,227 ± 367	427 ± 128	26.5
C4	2,007 ± 63	3,943 ± 1,177	35,51 ± 1,066	391 ± 146	26.1
C-row	1,920 ± 96	4,589 ± 522	4,160 ± 479	429 ± 47	26.3 ± 0.3
D1	1,907 ± 85	5,301 ± 442	4,812 ± 386	489 ± 119	26.5
D2	1,973 ± 44	5,990 ± 349	5,437 ± 250	552 ± 137	25.6
D3	2,037 ± 50	6,099 ± 968	5,517 ± 875	581 ± 162	26.8
D4	2,055 ± 58	5,697 ± 496	5,126 ± 471	571 ± 129	26.4
D-row	1,993 ± 67	5,771 ± 357	5,223 ± 322	548 ± 41	26.3 ± 0.5
E1	1,993 ± 38	7,490 ± 293	6,802 ± 180	688 ± 144	29.5
E2	2,063 ± 50	8,194 ± 1,233	7,421 ± 1,039	773 ± 252	27.7
E3	2,089 ± 15	7,280 ± 2,044	6,587 ± 1,897	692 ± 239	25.7
E4	2,059 ± 61	6,545 ± 1,191	5,903 ± 1,126	642 ± 175	26.5
E-row	2,051 ± 41	7,377 ± 679	6,678 ± 626	699 ± 54	27.4 ± 1.7
Average	1887 ± 141	4,835 ± 1,626	4,376 ± 1,479	459 ± 148	26.8 ± 1.2

Meyer, Egger et al.: The cellular organization of cortical barrel columns is whisker-specific

Supplementary methods: Detection of GAD67-positive somata

September 18, 2013

Contents

Chapter 1

Program flow

1.1 Calculate Brick Dimensions

Images are subdivided into bricks of 1024 x 1024 pixels with an overlap of 5%.

1.2 Statistical Analysis

This step detects bricks containing large amounts of bright pixels, e.g. barrels in L4, which contain a large number of inhibitory synapses around neuron somata. Some parameters in later steps are adjusted for this case to false-positive identification of these somata as GAD67-positive neurons.
For each brick, the histogram of the gray value distribution is computed, normalized to the maximum value and then integrated. Next, the mean m of all bricks in each section is computed. A brick is considered to contain large amounts of bright pixels (called "saturated" from this point on), if the integral of the normalized brick histogram is greater than $a \times m$. Usually, $a = 1$, but this can be adjusted if necessary.

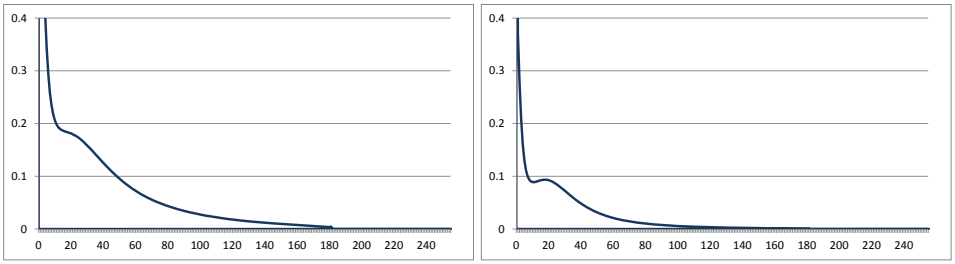

Figure 1.1: Normalized gray value histograms of two bricks within the same image stack.
Left: Saturated brick with histogram integral of 14.5
Right: Unsaturated brick with histogram integral of 6.2

1.3 Preprocessing

The pipeline of filters is illustrated in Figure 1.2.

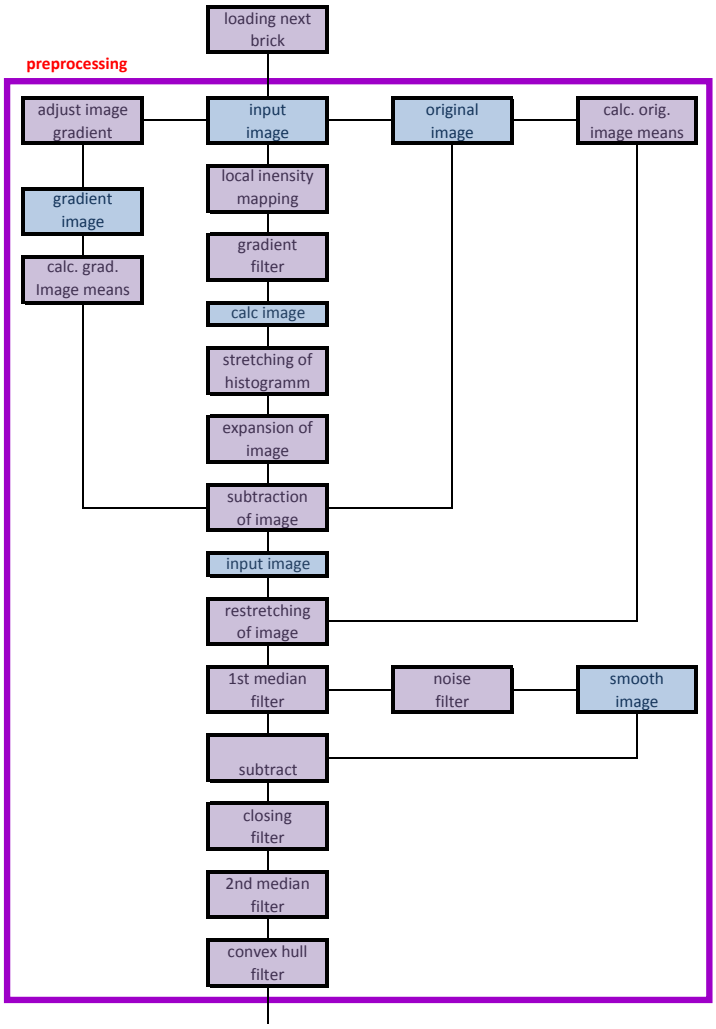

Figure 1.2: Program flow of preprocessing image filters

1.3.1 Compute Background Intensity Gradient

This step compensates for gradients in signal intensity across individual bricks.
For each optical section, a gradient image is computed by subdividing this image into $20 \times 20px$ large areas and computing the mean gray value in circles centered on these low-resolution coordinates (1.3 a). The resulting gray values are normalized to the range from 0 to 255 and interpolated to the full resolution image using Bicubic interpolation (1.3 b).
This pixel-wise background estimate I_{bg} and the mean background $I_{bg,mean}$ of the entire brick are used in the step 1.3.4.

1.3.2 Local Intensity Mapping

In this step, foreground pixel intensities are enhanced by a sigmoidal filter, as described previously (Oberlaender, Dercksen et al., J Neurosci Methods 2009).

1.3.3 Gradient Filter

The gradient magnitude of each optical slice is computed and normalized to a gray value range from 0 to 255. Before this normalization, the 8% of all pixels with the highest gray values are considered as saturated, set to 255 and not considered during calculation of the normalization factor.
Then, all pixel intensities are mapped with an exponential function:

$$I_{exp} = \exp(\gamma \times I_{old})$$

$$\gamma = \frac{\log(255)}{255}$$

1.3.4 Subtraction of Image

For each optical section, the exponential map is subtracted from the original image

$$I_{sub} = I_{original} - W \times I_{exp}$$

Here, the weight W is selected for each pixel individually based on the background intensity gradient and results in more uniform intensity across each optical section:

$$W = \begin{cases} 30 \times \left(\frac{I_{bg} - I_{bg,mean}}{255}\right)^2 & \text{if } I_{bg} > I_{bg,mean} \\ 1 & \text{otherwise} \end{cases}$$

The weight for saturated bricks is computed similarly:

$$W = \begin{cases} 40 \times C_f \left(\frac{I_{bg} - I_{bg,mean}}{255}\right)^2 & \text{if } I_{bg} > I_{bg,mean} \\ 1 & \text{otherwise} \end{cases}$$

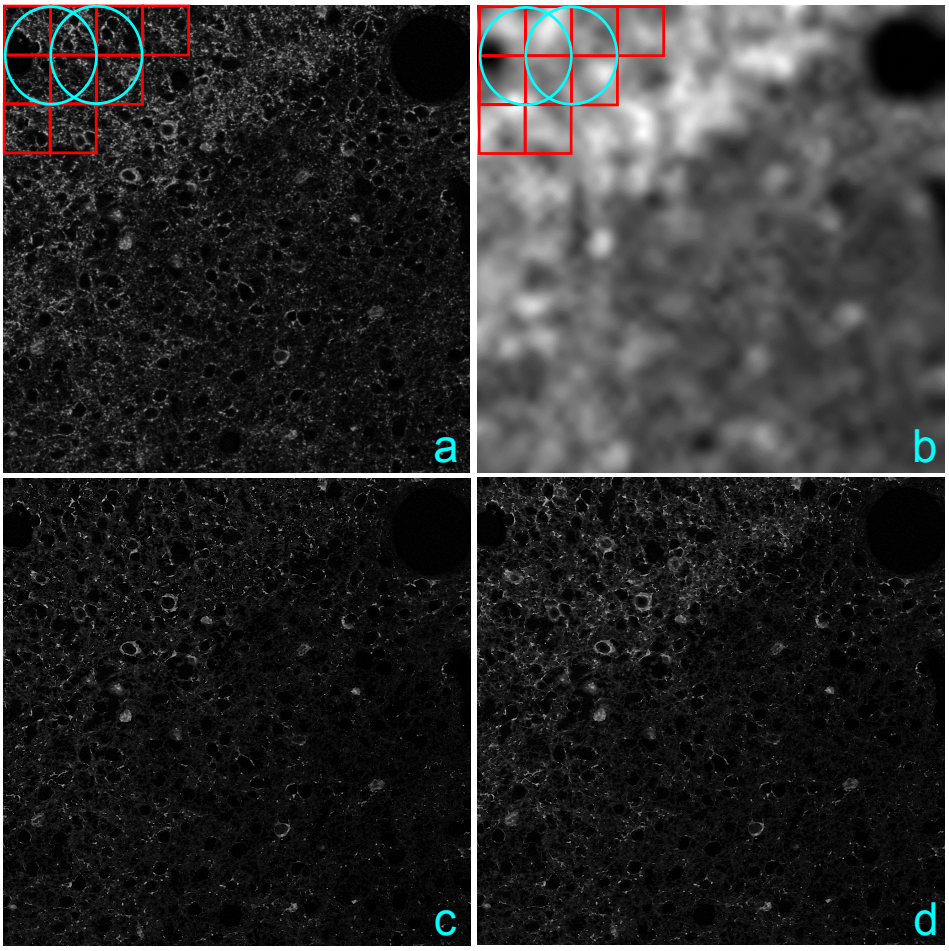

Figure 1.3: a: Image plane with low-resolution coordinates and corresponding circular areas used for calculation of mean gray values.
b: Resulting gradient image
c: Image plane after intensity gradient correction (see step 1.3.4).
d: Image plane without intensity gradient correction. Note higher overall intensity in upper left corner.

Here, C_f is the ratio of the histogram integral of the brick to the histogram integral threshold, as described in 1.2.

1.3.5 Restretching of Image

The gray value range of unsaturated bricks is again normalized from 0 to 255.
Next, for all bricks a lower threshold T is computed from the mean μ_B and standard deviation σ_B of all gray values of this brick.
For unsaturated bricks, the threshold is

$$T = f \times (\mu_B + \sigma_B)$$

For saturated bricks, the threshold is

$$T = f \times \left(\mu_B + \left[1 + \frac{C_f}{12}\right] \times \sigma_B\right)$$

C_f is the ratio of the histogram integral of the brick to the histogram integral threshold, as described previously.

The pixel-wise computed factor f takes varying brightness in individual optical sections into account:

$$f = \begin{cases} 1 + 2 \times \left(\frac{I_{bg} - I_{bg,mean}}{255}\right) & \text{if } I_{bg} > I_{bg,mean} + 1 \\ 1 & \text{otherwise} \end{cases}$$

Pixel gray values in unsaturated bricks are additionally mapped according to

$$I_{new} = I_{old} + \frac{155}{I_{old,MAX}} \times sin^4\left(\frac{\pi}{2} \times \frac{I_{old}}{255}\right)$$

If I_{new} is less than 12, it is set to 0; if I_{new} is greater than 255, it is set to 255.

1.3.6 Median Filter

The image is smoothed and small artifacts are removed with a median filter with a radius of $2px$.

1.3.7 Noise Filter

In this step, the standard deviation I_{STD} in a neighborhood with radius $1px$ around each pixel is computed and mapped according to $I_{border} = (I_{STD})^{1.5}$ and then normalized to an intensity range from 0 to 255.
This image contains mainly the borders of all bright objects.

1.3.8 Subtract

The image containing the borders is now subtracted from the image according to $I_{new} = I_{old} - \frac{1}{2} I_{border}$. Gray values less then 20 are set to 0. This step eliminates small noise objects and reduces medium-sized noise objects in gray value intensity and size.

1.3.9 Closing Filter

Next, a morphological gray scale closing with a radius of $2px$ is applied to the image. This removes small gaps in GAD67-positive neuron somata that may have been introduced in the previous step.

1.3.10 2nd Median Filter

Remaining small artifacts are remove by a second median filter with a radius of $2px$.

1.3.11 Convex Hull Filter

In this step, GAD67-positive somata are reconstructed in 3D. First, each optical section is turned into a binary image by computing all connected components with gray values > 100 and size between 130 and 2,500 pixels. For all remaining connected components, the convex hull is computed, connected by lines with a thickness of $3px$ and unlabeled pixels within the convex hull are labeled as foreground.
This is repeated in order to connect possibly fragmented parts of a single GAD67-positive neuron soma.
Now, for every convex object the number of consecutive optical sections in which this object is present is determined (i.e., the number of optical sections in which convex objects are present which are connected in the z-direction). Objects that occur in less than $S_{min} = 0.06 \times N + 0.8$ sections are discarded as false-positives. Here, N is the total number of optical sections.

The resulting binary objects are split into single neurons as described in (4).

1.4 Delete Clusters with multiple Landmarks

In regions of high GAD67-positive bouton densities, large neuron somata with a high number of perisomatic GAD67-positive boutons may lead to false detection of several small GAD67-positive neuron somata (1.8). In order to correct for this systematic error, all detected GAD67-positive neuron somata are assumed as corresponding to a NeuN-positive neuron soma if the distance between them is less than $20px$. Only if the total size of the NeuN-positive neuron soma is less than $25,000px$, the maximal XY-area of this soma is less than $2,5000px$ and there are at most 2 detected GAD67-positive neuron somata associated with this neuron soma, it is considered a true GAD67-positive neuron soma; otherwise it is deleted.

1.5 Cylindrical Position Correction

Because the convex hull of GAD67-positive neuron somata is computed on individual optical sections, it may occur that a single GAD67-positive neuron is split into 2 or more clusters (1.9). This error is corrected by computing a cylinder with a radius of $6\mu m$ and height of $20\mu m$ around every computed landmark. If there are other landmarks within this volume, they are considered to belong to the same neuron and a new landmark is computed by averaging the 3D positions of the corresponding landmarks.

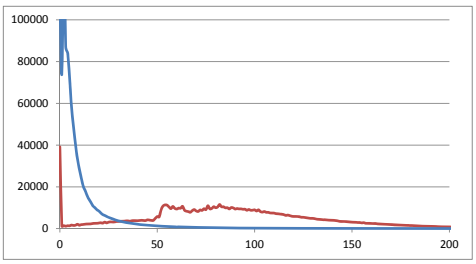

Figure 1.4:
red: gray value histogram of gradient magnitude-filtered image
blue: gray value histogram after normalization and exponential mapping of gray values

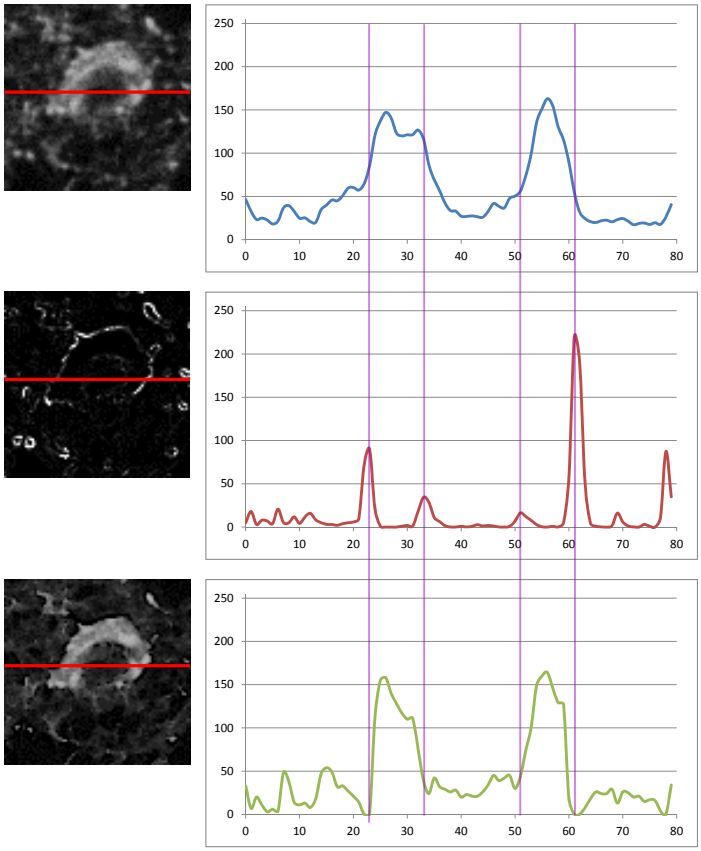

Figure 1.5:
Top: Pixel intensities along the red line across a GAD67-positive neuron soma in the original image.
Center: Pixel intensities along the same line in the gradient-filtered image. Note that only the outline of the GAD67-positive neuron soma and GAD67-labeled boutons are visible.
Bottom: Resulting pixel intensities after subtraction of images (1.2). Note that the GAD67-positive neuron soma is preserved, while small GAD67-positive boutons are removed from the image.

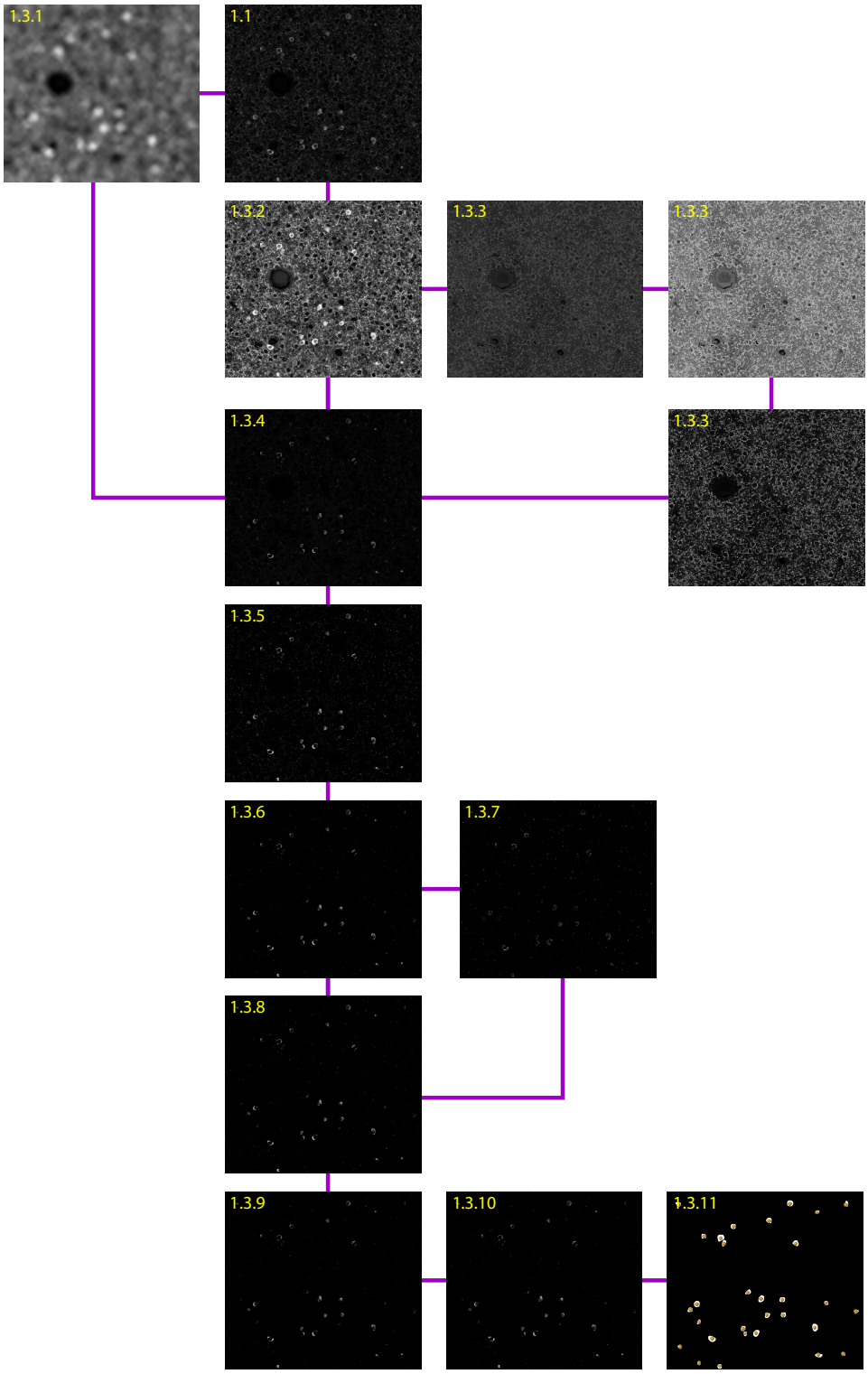

Figure 1.6: Effect of the individual processing steps on one example brick. In the last image, the detected landmarks are added.

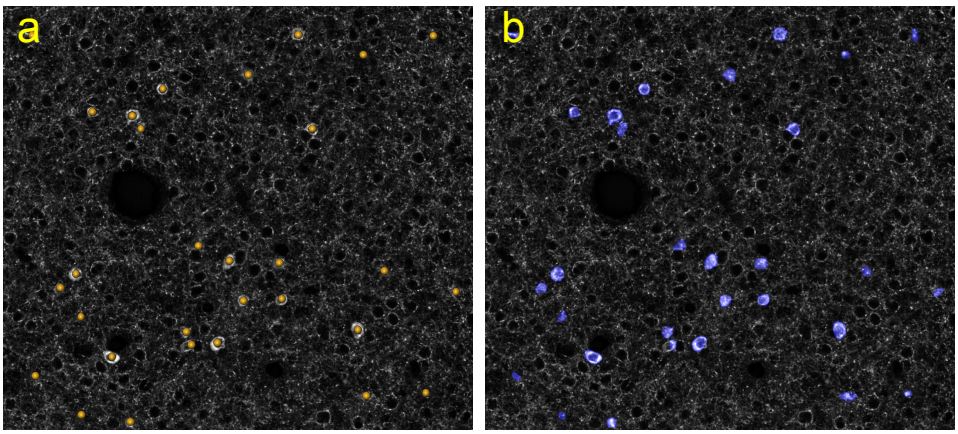

Figure 1.7:
a: original image with final detected landmarks.
b: original image with computed convex hulls.

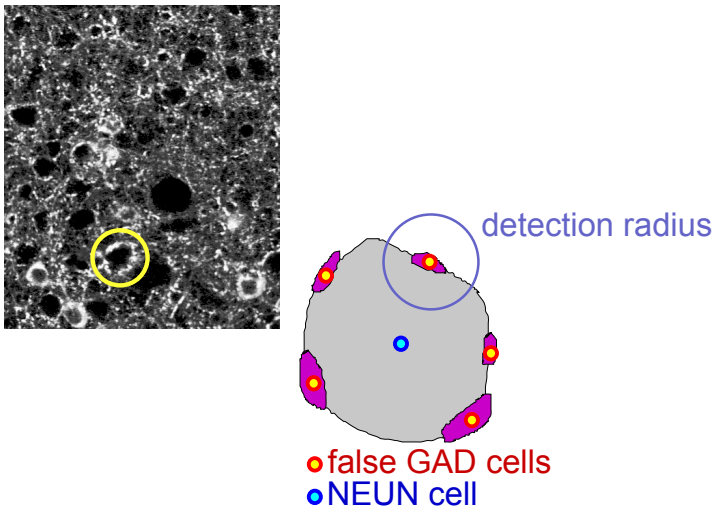

Figure 1.8: Left: Example of a large NeuN-positive, GAD67-negative neuron soma with a large number of perisomatic GAD67-positive boutons (yellow circle). Right: Systematic correction of false-positive GAD67 clusters.

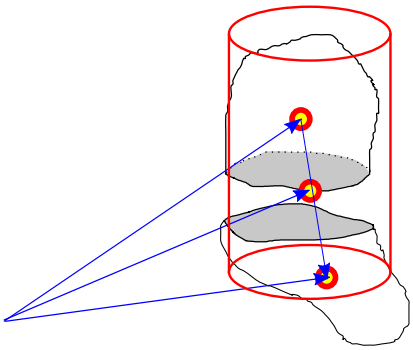

Figure 1.9: Cylindrical Position Correction.

Chapter 2

Validation

2.1 Parameter optimization

All parameters used during preprocessing were systematically tested by comparing the results of the automated detection with manually detected GAD67-positive neuron somata (here, also referred to as somata).
We randomly selected 23 bricks of 1024×1024 pixels size (approx. $370\mu m \times 370\mu m$) from 8 different sections across all cortical layers from one animal. An expert user manually placed landmarks at the locations of all somata. The total number of manually detected somata was 1331, compared with 1303 automatically detected somata. Thus, the relative counting error is 2.2%, similar to previously reported results for NeuN-positive somata (4).
The false-positive (FP) and false-negative (FN) error rates were 32% and 33%, respectively, measured with a correspondence distance of $5\mu m$ (i.e., less than the typical soma size).
We determined the accuracy of the automated soma detection at the typical spatial resolution used in this study by measuring the distance of each automatically detected GAD67-positive soma to the nearest NeuN-positive soma. Then, we counted how many GAD67-positive somata did not have a nearest neighbor within a fixed radius. For radii of $50\mu m$ and $100\mu m$, these values were 12% and 5%, respectively.

2.2 Robustness

To test the robustness of the optimized parameter set, we additionally validated the automated method on manual counts of a nearly complete tangential section (approx. $3mm \times 4mm$). The relative counting error was 3% (total number of somata: 1990), with FP and FN error rates of 22% and 19%, respectively.

2.3 Inter-animal variability

Due to different staining and illumination conditions, we corrected for systematic differences in counting results across the three different animals.
We computed the average vertical density profile for GAD67-positive somata in the C2, D2 and D3 columns. Comparison with results from manual counts of these columns (3) resulted in a depth-dependent correction factor that was applied to the vertical density profile of all columns, taking varying cortical thickness into account.
The average correction factor was 1.46.

Supplementary References

1. Oberlaender M, *et al.* (2012) Cell Type-Specific Three-Dimensional Structure of Thalamocortical Circuits in a Column of Rat Vibrissal Cortex. *Cerebral cortex (New York, NY : 1991).*
2. Meyer HS, *et al.* (2010) Number and laminar distribution of neurons in a thalamocortical projection column of rat vibrissal cortex. *Cereb Cortex* 20(10):2277-2286.
3. Meyer HS, *et al.* (2011) Inhibitory interneurons in a cortical column form hot zones of inhibition in layers 2 and 5A. *Proc Natl Acad Sci U S A* 108(40):16807-16812.
4. Oberlaender M, *et al.* (2009) Automated three-dimensional detection and counting of neuron somata. *J Neurosci Methods* 180(1):147-160.